nature physics

Article

https://doi.org/10.1038/s41567-023-02346-3

Raman sideband cooling of molecules in an optical tweezer array

Received: 5 June 2023

Accepted: 21 November 2023

Published online: 22 January 2024



Check for updates

Yukai Lu 12.3, Samuel J. Li 13. Connor M. Holland 13.4 Lawrence W. Cheuk © 1 🖂

Ultracold molecules have been proposed as a candidate platform for quantum science and precision measurement because of their rich internal structures and interactions. Direct laser-cooling promises to be a rapid and efficient way to bring molecules to ultracold temperatures. However, for trapped molecules, laser-cooling to the quantum motional ground state remains an outstanding challenge. A technique capable of reaching the motional ground state is Raman sideband cooling, first demonstrated in trapped ions and atoms. Here we demonstrate Raman sideband cooling of CaF molecules trapped in an optical tweezer array. Our protocol does not rely on high magnetic fields and preserves the purity of molecular internal states. We measure a high ground-state fraction and achieve low motional entropy per particle. The low temperatures we obtain could enable longer coherence times and higher-fidelity molecular qubit gates, desirable for quantum information processing and quantum simulation. With further improvements, Raman sideband cooling will also provide a route to quantum degeneracy of large molecular samples, which could be extendable to polyatomic molecular species.

Ultracold molecules have been proposed as a new platform for exploring many areas in physics ranging from simulation of quantum many-body Hamiltonians, to quantum information processing, to precision measurements in searches for physics beyond the Standard Model¹⁻⁴. Yet, cooling and fully controlling molecules have been long-standing experimental challenges. One route to produce ultracold molecules is through assembly from atoms, for which cooling techniques are well developed. This approach has successfully been used to produce bialkali molecules, enabling explorations in ultracold chemistry^{5,6} and the creation of quantum-degenerate molecular gases well suited for studying long-range interacting many-body systems^{7,8}.

In contrast to assembly from ultracold atoms, methods that directly cool could be broadly applicable to a large variety of molecular species, including polyatomic ones. In particular, direct laser-cooling of molecules has seen great advances recently. Starting with molecular magneto-optical traps near the Doppler limit of ~100 μK (refs. 9-13), sub-Doppler cooling techniques have allowed experiments to enter into the μK regime^{10,13–19}. Importantly, sub-Doppler cooling has enabled optically trapped molecular samples with record densities 14,18,20 and arrays of single molecules trapped in optical tweezers²¹⁻²³.

Access to molecular samples at even lower temperatures could enable new possibilities. For example, molecular tweezer arrays have recently emerged as a promising platform for quantum science. Notably, recent work has shown high-fidelity control over molecular positions and internal states, coherent dipolar interactions and implementation of an entangling two-qubit gate^{22,23}. Yet residual thermal motion limits the achievable coherence times and gate fidelities^{22–24}. These limitations can be largely eliminated by cooling to the motional

One technique capable of cooling to the motional ground state is Raman sideband cooling (RSC)²⁵. First, a Raman process transfers a molecule initially in internal state $|\uparrow\rangle$ to $|\downarrow\rangle$ while removing Δn quanta of motional energy. Subsequently, optical pumping reinitializes the internal state to $|\uparrow\rangle$ while largely preserving the motional state. By iterating over these two steps, cooling is achieved. RSC was first proposed and demonstrated for trapped ions and atoms in optical

Department of Physics, Princeton University, Princeton, NJ, USA. Department of Electrical and Computer Engineering, Princeton University, Princeton, NJ, USA. ³These authors contributed equally: Yukai Lu, Samuel J. Li, Connor M. Holland. 🖂 e-mail: lcheuk@princeton.edu

lattices $^{26-28}$ and has since been used to cool single atoms in tweezer traps to their motional ground states 29,30 , for imaging in quantum gas microscopes 31,32 and to produce single molecules by means of assembly from two RSC-cooled atoms $^{33-35}$. RSC also provides a rapid and efficient (low-loss) all-optical method to create atomic Bose–Einstein condensates 36,37 , circumventing the need for evaporation.

Raman sideband cooling of optically trapped and laser-cooled molecules faces two main challenges that arise from the complex internal structure of molecules³⁸. First, state-dependent optical trapping leads to inhomogeneous broadening of Raman transitions, preventing resolved addressing of cooling sidebands and decreasing transfer efficiency. Second, efficient optical pumping is difficult because of the large number of molecular states and the degradation of free-space selection rules in deep optical traps.

In this work, we demonstrate RSC of molecules for what we believe to be the first time. We overcome the above challenges by devising an RSC scheme for CaF molecules that provides both narrow Raman transitions and efficient optical pumping. Our scheme does not require high magnetic fields, in contrast to the one proposed in 38. In addition, it preserves internal molecular state purity, which is crucial for applications in quantum information processing and quantum simulation of many-body systems.

Our work begins with single CaF molecules that are cooled by Λ -enhanced grey molasses ¹⁴ and trapped in a one-dimensional (1D) array of linearly polarized optical tweezers ^{21,22,39}. Raman beams are sent along the radial and axial directions and are near-detuned from the X^2 $\Sigma(v=0,N=1) \rightarrow B^2\Sigma(v=0,N=0)$ transition at 531 nm (Fig. 1). Optical pumping is achieved on the $X^2\Sigma(v=0,N=1) \rightarrow A^2\Pi_{1/2}(v=0,J=1/2,+)$ transition at 606 nm.

We identify a suitable pair of internal states $\{|\uparrow\rangle, |\downarrow\rangle\}$ for RSC. Constrained by optical pumping, we consider optically cyclable states from $X^2\Sigma(v=0, N=1)$. In free space, selection rules enable optical pumping into the stretched states $|\pm\rangle = |N=1, J=3/2, F=2, m_F=\pm 2\rangle$. Specifically, the state $|+\rangle(|-\rangle)$ is dark to $\sigma_+(\sigma_-)$ and π light addressing the $X^{2}\Sigma(v=0, N=1) \rightarrow A^{2}\Pi_{1/2}(v=0, J=1/2, +)$ transition. In deep tweezer traps, the trapping light can admix in bright states and modify selection rules, degrading optical pumping. The admixture can be reduced by providing a well-defined quantization axis with a magnetic field **B** along the polarization axis of the trapping light 30,38. However, at certain fields, because of tensor a.c. Stark shifts, level crossings can occur, increasing bright state admixtures. Our calculations indicate that $|\uparrow\rangle = |-\rangle$ is immune from these crossings at low fields and over a large range of trap depths, therefore robustly providing low bright state admixtures (Supplementary Information Section I). In particular, the bright state population admixture remains below 10⁻⁴ even for traps as deep as $k_{\rm B} \times 2$ mK at B = 4.4 G, where $k_{\rm B}$ is the Boltzmann constant.

For $|\downarrow\rangle$, we seek a state that is connected by a two-photon Raman transition to $|\uparrow\rangle$ and has minimal differential a.c. Stark shifts with $|\uparrow\rangle$. Our calculations indicate that $|\downarrow\rangle = |N=1, J=3/2, F=1, m_F=0\rangle$ satisfies these requirements. In particular, although most N=1 states experience fractional differential a.c. Stark shifts at the 10^{-1} level (absolute differential shift divided by the mean shift), those between $|\uparrow\rangle$ and $|\downarrow\rangle$ are suppressed to 10^{-2} even in deep traps with depths $-k_B\times 1$ mK. The shifts can be further reduced by changing the angle θ between **B** and the tweezer polarization, with 10^{-3} fractional shifts possible at specific 'magic' angles. For example, at a trap depth of $k_B\times 0.3$ mK and magnetic field of B=5.5 G, the magic angle is $\theta\approx 57^\circ$.

We experimentally verify the properties of $\{|\uparrow\rangle,|\downarrow\rangle\}$ through Raman spectroscopy and optical pumping dynamics. We first probe the inhomogeneous broadening of Raman transitions arising largely from differential Stark shifts. At a trap depth $U=k_{\rm B}\times326(7)~\mu{\rm K}$, we measure the linewidth Γ of the carrier ($\Delta n=0$) transition using copropagating Raman beams. We prepare molecules in $|\uparrow\rangle$ and measure the population in $|\downarrow\rangle$ (P_{\downarrow}) versus $\delta_{\rm c}$, the two-photon detuning from the carrier frequency. At $\theta=0^{\circ}$ and B=4.4 G, we measure a linewidth of

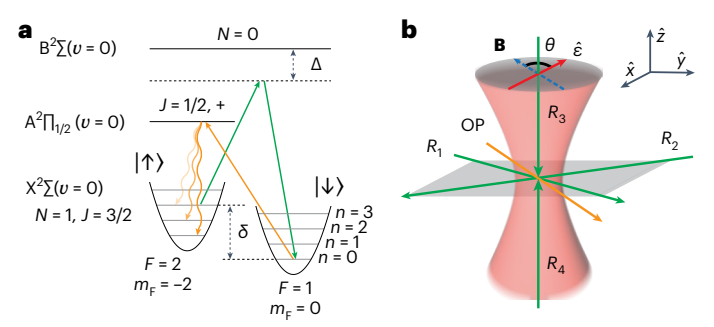


Fig. 1 | **Raman sideband cooling scheme. a**, Motional-changing two-photon Raman transitions between |↑⟩ and |↓⟩ are driven using laser beams detuned by $\Delta \approx -2\pi \times 42$ GHz from the $X^2\Sigma(\nu=0,N=1) \rightarrow B^2\Sigma(\nu=0,N=0)$ transition at 531 nm. δ denotes the two-photon detuning. Optical pumping into |↑⟩ is performed using light addressing the $X^2\Sigma(\nu=0,N=1) \rightarrow A^2\Pi_{1/2}(\nu=0,J=1/2,+)$ transition at 606 nm. **b**, A magnetic field **B** is applied in the radial plane, and is oriented at an angle of θ relative to the polarization axis of the tweezer light ($\epsilon \parallel \hat{x}$). **B** defines the quantization axis. Raman laser beams R_1 , R_2 (R_3 , R_4) address the radial (axial) directions. R_1 and R_2 are optionally retro-reflected to address two orthogonal radial directions. Optical pumping light (OP) is applied radially.

 Γ = 2π × 26.5(3) kHz. This is below the radial trapping frequency ω_r = 2π × 117.3(4) kHz, allowing radial sidebands ($\Delta n \neq 0$) to be resolved. At B = 5.5 G, as a function of θ , we find that Γ reaches a minimum of -2π × 7 kHz at the magic angle of θ_m = 56.3(3)°, as predicted (Fig. 2a). Notably, at θ_m , $\hbar\Gamma/U \approx 10^{-3}$, and the linewidth Γ is below the axial trapping frequency $\omega_z \approx 2\pi \times 26$ kHz, allowing axial sidebands to be resolved (Supplementary Information Section IV).

Next, we measure optical pumping dynamics. Starting with molecules initially distributed over all 12 hyperfine states of $X^2\Sigma(v=0, N=1)$, we measure the $|\uparrow\rangle$ population (P_{\uparrow}) after variable durations of optical pumping. At short times, P_{\uparrow} increases as molecules are pumped into $|\uparrow\rangle$ and subsequently saturates to P_s , the final population value. At long times, P_{\uparrow} decreases because of molecular loss arising from heating or decay into undetected states due to imperfect darkness of $|\uparrow\rangle$ (Fig. 2b). The darkness of $|\uparrow\rangle$, essential for efficient optical pumping, can therefore be quantified by the figure-of-merit $\kappa = \tau_2/\tau_1$, where $\tau_1(\tau_2)$ is the 1/erise (fall) time of P_{\uparrow} . P_{s} provides a complementary measure of optical pumping efficiency. When $\theta = 0^{\circ}$ and B = 4.4 G, $\kappa \approx 8 \times 10^{3}$ and $P_{s} \approx 0.8$, even at a deep trap depth of $k_B \times 930(20) \mu K$ (Fig. 2c). In comparison, in the magic configuration ($\theta = \theta_m$, B = 5.5 G), we find that both κ and P_s decrease with increasing trap depth, indicating degrading selection rules. For all tweezer depths explored, κ is a factor of 6 to 20 lower than that at $\theta = 0^\circ$. This shows that optimal optical pumping (at $\theta = 0^\circ$) and Raman linewidths (at $\theta = \theta_m$) cannot be simultaneously achieved.

For RSC, deep tweezer depths help preserve the motional state during optical pumping, which is critical for cooling. Although the magic configuration at $\theta_{\rm m}$ provides the narrowest Raman transitions, optical pumping is severely degraded at deep depths. On the other hand, at $\theta=0^{\circ}$, optical pumping is efficient even in deep tweezers. The Raman linewidth is slightly broader, but sufficient to resolve the radial sidebands. We therefore choose to perform Raman cooling at $\theta=0^{\circ}$.

We next verify Raman motional coupling by driving sideband transitions at $\theta=0^\circ$. The Raman coupling between different motional states is characterized by the Lamb–Dicke parameter $\eta=|\Delta \mathbf{k}|l/\sqrt{2}$, where $\Delta \mathbf{k}$ is the difference in wave-vectors between the two Raman beams and $l=\sqrt{\hbar/(m\omega)}$ is the harmonic oscillator length, m being the molecular mass and ω the trapping frequency. With molecules initially prepared in $|\uparrow\rangle$, we probe radial and axial motional state transfer at $U=k_{\rm B}\times 326(7)~\mu{\rm K}$, $B=4.4~{\rm G}$. We pulse on Raman beams and measure P_{ν} versus $\delta_{\rm c}$ (see Methods for Raman beam and pulse parameters). The radial Lamb–Dicke parameter is $\eta_{\rm r}=0.46$ at this depth, allowing us to observe resolved radial sidebands at $\delta_{\rm c}=(\Delta n_{\rm r})\omega_{\rm r}$ up to $|\Delta n_{\rm r}|=4$ (Fig. 3a), where $\omega_{\rm r}=2\pi\times 117.3(4)~{\rm kHz}$. Axially, the weaker confinement leads to

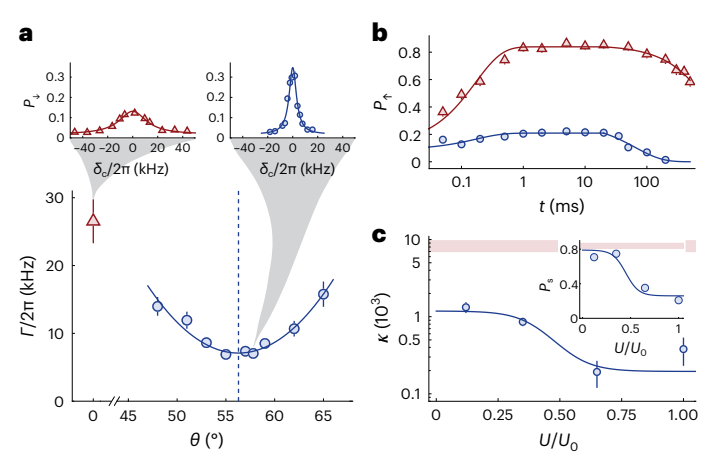


Fig. 2 | Raman linewidths and optical pumping characterization. a, Raman linewidths Γ versus θ , measured at a tweezer depth of $k_{\rm p} \times 326(7)$ uK. Γ is smallest at the magic angle $\theta_m = 56.3(3)^\circ$, indicated by the dashed vertical line. Representative spectra along with their Lorentzian fits (solid) are shown in the sub-panels. δ_c denotes the two-photon detuning from the carrier transition. **b**, $|\uparrow\rangle$ population P_{\uparrow} versus optical pumping time t at a tweezer depth of $k_{\rm R} \times 930(20)$ uK. Red triangles (blue circles) show data for $\theta = 0^{\circ} (\theta = \theta_{\rm m})$. Solid curves show simultaneous fits to the early and late time dynamics. The measured values of P_{\uparrow} are affected by the initial state preparation efficiency, the detection efficiency and finite lifetime due to vacuum and blackbody loss. These factors account for -10% of the population. ${f c}$, The figures-of-merit ${f \kappa}$ and ${f P}_{\rm s}$ at ${f heta}_{\rm m}$ versus trap depth U/U_0 ($U_0 = k_B \times 930(20) \mu K$) are shown by blue circles, with solid lines as guides to the eye. The corresponding values for $\theta = 0^{\circ}$ are shown by the red shaded regions and indicate substantially better optical pumping. For the top panels in a and for b, plot markers and error bars represent mean values and standard errors of the mean (s.e.m.), respectively. Each data point is obtained from 700 (a) and 300 (b) loaded tweezers. For the bottom panel in a and for c, the markers represent mean values and the error bars correspond to propagated errors from 1σ uncertainty of corresponding curve fits.

a larger Lamb–Dicke parameter of $\eta_z = 1.34$, allowing substantial motional coupling up to $|\Delta n_z| \approx 10$ (Fig. 3b). We observe that the axial spectrum is substantially broader than the measured carrier Raman linewidth, indicating that motion-changing Raman transfers are indeed occurring. The centre of the axial spectrum is also substantially shifted from the carrier frequency. This shift corresponds to the photon recoil shift present in free-space two-photon Doppler spectroscopy (Supplementary Information Section V).

Having demonstrated motional state-changing Raman transfer, we next construct a radial cooling sequence consisting of two discrete steps: optical pumping and Raman transfer on a cooling ($\Delta n < 0$) sideband. We optically pump at a deep tweezer depth of $U_0 = k_B \times 930(20) \,\mu\text{K}$ to minimize increase in motional quanta (see Methods for optical pumping parameters). Because of the large number of hyperfine states that are accessed during optical pumping (12 states in the optically cyclable N = 1 rotational manifold), our simulations indicate that ~19 optical pumping photons are required (Supplementary Information Section II). Each optical pumping step therefore increases the motional energy of a molecule by an equivalent of $\Delta n_{\rm r}^{\rm op} \approx 1.3$ radial quanta (Supplementary Information Section II). To attain net cooling, we therefore address the $\Delta n_r = -2$ sideband. To obtain sufficient motional coupling and reduce inhomogeneous broadening, we perform Raman transfer at a reduced tweezer depth $U_R = k_B \times 326(7) \mu K$ (see Methods for Raman beam configuration and parameters), the same depth where we measured Raman linewidths. Each cooling cycle has a duration of 0.65 ms and the trap depths are ramped adiabatically over 0.2 ms between U_0 and U_R (Fig. 3c).

To verify cooling, we first indirectly probe the temperature by means of adiabatic reduction of the tweezer depth^{40,41}. Hot molecules

are spilled progressively as the trap is lowered. At a fixed final trap depth $U_{\rm spill}$, the surviving fraction f increases with lower temperatures. After 90 cycles of radial cooling (RC), we indeed observe that f increased, indicating cooling (Fig. 3d). We next add axial cooling by switching on extra axial Raman beams with the same two-photon detuning. Owing to limitations in our experimental setup, the radial and axial Raman beams cannot be independently controlled. They are therefore switched on simultaneously and constrained to a single common two-photon detuning. The combined radial/axial cooling (RAC) sequence simultaneously addresses the $\Delta n_{\rm r} = -2$ radial and the $\Delta n_z \approx -9$ axial sidebands (see Methods for Raman beam configuration and parameters). We find that f increased after 90 cycles of RAC, compared with the same number of radial cooling cycles (Fig. 3d), indicating successful cooling in all directions.

The cooling rate of RAC can be probed by measuring f versus the number of cooling cycles N. Fixing $U_{\rm spill}=k_{\rm B}\times 0.72(2)~\mu{\rm K}$, we find a 1/e cooling timescale of $N_{\rm c}=51(14)$ cycles. We also quantify loss during cooling. With Raman and optical pumping beams off, but keeping the tweezer depth ramps, we observe a 1/e lifetime of $1.28(15)\times 10^3$ cycles. Remarkably, with Raman cooling on, the lifetime increases to $2.7(4)\times 10^3$ cycles, corresponding to a fractional loss of $3.66(6)\times 10^{-4}$ per cycle. This difference could arise from Raman cooling compensating for technical heating, or from Raman beams repumping molecules that decay into $X^2\Sigma(v=0,N=3)$ due to off-resonant scattering of tweezer light 3^3 .

Although adiabatic trap reduction provides qualitative evidence of three-dimensional cooling, it does not directly provide a quantitative temperature. For thermometry, we rely on Raman spectroscopy.

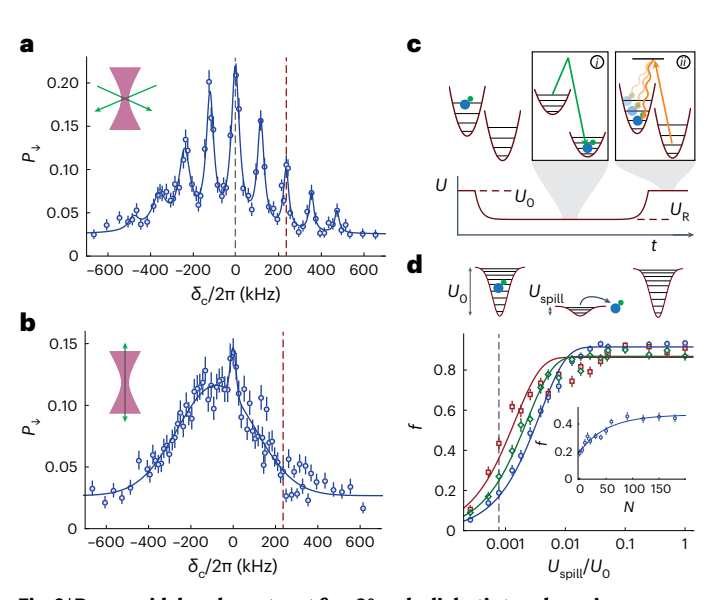


Fig. 3 | Raman sideband spectra at $\theta = 0^{\circ}$ and adiabatic trap lowering curves. **a**, Population transfer P_{\downarrow} using radial Raman beams versus δ_{c} , the two-photon detuning from the carrier ($\Delta n = 0$). The solid blue line shows a fit using a sum of nine Lorentzians with an offset. The black (red) dashed line marks the carrier $(\Delta n_r = -2 \text{ sideband})$. **b**, Population transfer P_{\downarrow} using axial Raman beams versus δ_c . Solid curve is a guide to the eye. The red dashed line shows the two-photon detuning from the carrier $\delta_c = 2\omega_r$ used during cooling. c, Raman cooling sequence consists of (i) Raman transfers at a tweezer depth of $U_R = k_B \times 326(7) \,\mu\text{K}$ and (ii) optical pumping at a higher depth of $U_0 = k_B \times 930(20) \,\mu\text{K}$. **d**, Probing $temperature\ by\ means\ of\ adiabatic\ trap\ lowering.\ The\ tweezer\ depth\ is\ lowered$ to U_{spill} over 1 ms, held 10 ms to allow hot molecules to escape and increased back to full depth for detection. The surviving fraction f versus U_{spill}/U_0 is shown for no cooling (blue circles), radial cooling (RC) (green diamonds) and radial/axial cooling (RAC) (red squares). Inset, f versus number of RAC cycles N at a fixed lower depth $U_{\text{spill}} = k_{\text{B}} \times 0.72(2) \,\mu\text{K}$ (dashed line in main plot). For all plots, the markers represent mean values and error bars represent s.e.m. Each data point is obtained from 1,000 (a and b) and 400 (d) loaded tweezers.

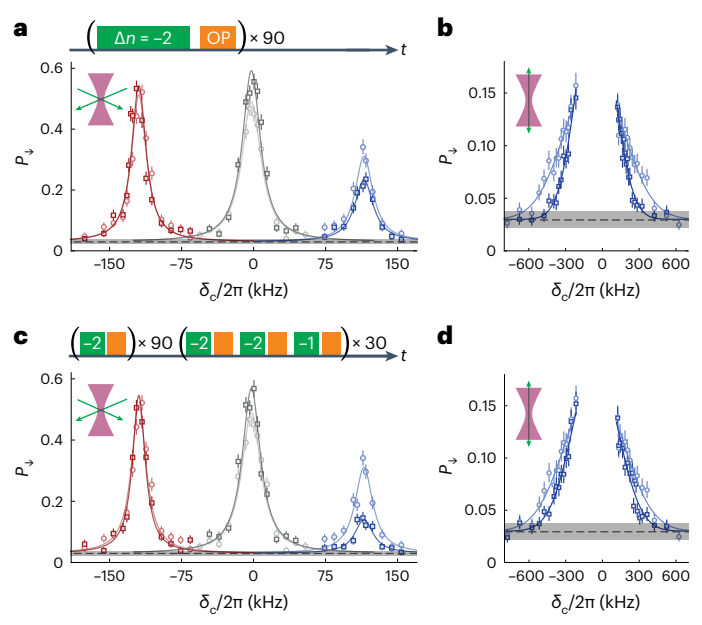


Fig. 4 | **Raman thermometry. a, c**, Radial Raman spectra showing the carrier along with $\Delta n_r = \pm 1$ sidebands. Grey squares and light grey circles show the carrier after and before cooling, respectively. Red (blue) squares show the $\Delta n_r = 1$ ($\Delta n_r = -1$) sideband after cooling; light red (light blue) circles show the $\Delta n_r = 1$ ($\Delta n_r = -1$) sideband before cooling, **b, d**, Unresolved axial Raman spectra. Blue squares (light blue circles) show spectra after (before) cooling. **a, b**, Spectra after 90 cycles of RAC (darker colours) compared with spectra before Raman cooling (lighter colours). **c, d**, Spectra after 90 cycles of RAC and 30 cycles of IRC (darker colours) and spectra before Raman cooling (lighter colours). For radial (axial) data, solid lines show fits to Lorentzian (Gaussian) distributions with a vertical offset. For all panels, the dashed lines show the independently measured offset without Raman beams; the shaded region represents the 1 σ standard errors obtained from 1,800 loaded tweezers. For all plots, the markers represent mean values and the error bars represent s.e.m. Each data point is obtained from 500 (**a,c**) and 1,000 (**b,d**) loaded tweezers.

We first cool at $\theta = 0^{\circ}$ and then perform spectroscopy in the magic configuration ($\theta = \theta_m$ and B = 5.5 G) to minimize Raman broadening. Along the radial direction, the $\Delta n_r = \pm 1$ sidebands are well resolved. Given the radial Lamb-Dicke parameter and the temperature regime, the Raman motional coupling depends weakly on the motional state n_r (Supplementary Information Section V). This allows us to observe coherent $\Delta n_r = \pm 1$ sideband transfer and also simplifies interpretation of spectra (Supplementary Fig. 6). We apply π -pulses and measure the resulting transfer around each sideband (Fig. 4a). The ratio \mathcal{A} between the peak transfer fractions of the heating and the cooling sidebands allows us to extract 1D ground state fractions and temperatures (Supplementary Information Section V). Assuming either uniform motional coupling or thermal occupation, we find a 1D radial ground state fraction of $P_0 = 1 - 1/A = 0.60(6)$ after RAC. Assuming only a thermal distribution, the mean radial motional occupation \bar{n}_r is given by $\bar{n}_{\rm r}=1/(\mathcal{A}-1)$. We find $\bar{n}_{\rm r}=0.66\,(16)\,(\text{dimensionless temperature})$ of $\tilde{T}_r = k_B T_r / (\hbar \omega_r) = 1 / \ln(A) = 1.1(2)$), compared with $\bar{n}_r = 1.4(4)$ $(\tilde{T}_r = 1.8(5))$ before cooling.

We probe the axial temperature similarly. Although we can observe resolved axial sidebands spaced up to $|\Delta n_z|\approx 10$, extracting a temperature is difficult because of the complex lineshape arising from high axial temperatures and a large Lamb–Dicke parameter (Supplementary Information Section V). Nevertheless, robust thermometry is possible by probing high-order sidebands in the unresolved regime 30,42 . The wings of the spectra become Gaussian, and the spectra can be understood as Doppler-sensitive two-photon transfer (Supplementary

Information Section V). By fitting the wings, one can robustly extract a temperature. Experimentally, we increase the Raman Rabi coupling such that the wings of the spectra appear smooth (Fig. 4b). Fitting the spectra gives an axial temperature of $\tilde{T}_z = k_{\rm B} T_z / (\hbar \omega_z) = 7.5^{+1.0}_{-0.7}$ ($\bar{n}_z = 7.0^{+1.0}_{-0.7}$) after RAC, compared with $\tilde{T}_z = 26.5^{+4.0}_{-3.1}$ ($\bar{n}_z = 26.4^{+4}_{-3.1}$) before cooling.

Lastly, we demonstrate a way to reach even lower temperatures. In our RAC scheme, because $\Delta n_{\rm r}=-2$ sidebands are addressed, molecules can accumulate in $n_{\rm r}=1$, limiting the radial ground state fraction. To circumvent this while maintaining net cooling, we apply an extra radial cooling sequence, in which we interlace radial cooling cycles that separately address the $\Delta n_{\rm r}=-2$ and $\Delta n_{\rm r}=-1$ sidebands (Fig. 4c). With further 30 cycles of interlaced radial cooling (IRC), we observe that the 1D radial ground state fraction increases to $P_0=0.79(4)$, corresponding to an average radial occupation of $\bar{n}_{\rm r}=0.27(7)$ ($\tilde{T}_{\rm r}=0.65(9)$). Because the axial direction is not cooled during IRC, the axial temperature increases to $\tilde{T}_z=13.5(14)$ ($\tilde{n}_z=13.0(14)$), still below the initial temperature.

When the motion is highly quantized, as in our case, a useful figure-of-merit in addition to temperature is the motional entropy. This quantifies how many motional states are populated and indicates the level of control over the initial motional state. With RAC, we obtain a motional entropy per particle of $s = 5.2^{+0.5}_{-0.4}$ compared with $s = 7.5^{+0.8}_{-0.7}$ before cooling. With IRC, we further reduce the motional entropy per particle to s = 4.9(3), the lowest reported so far for laser-cooled molecules. As most of the entropy is in the axial motion, lower entropies and temperatures could be reached with increased axial confinement. Separately, improved implementations of our cooling scheme that offer independent intensity and frequency control of the Raman beams could allow lower temperatures to be reached. In short, these capabilities allow one to avoid interference between multiple Raman beams, which causes additional broadening that currently limits our achieved temperatures (Supplementary Information Section VI). Independent Raman beam control will also allow the use of optimized Raman pulse sequences such as those that address progressively lower sidebands⁴²⁻⁴⁴. These sequences could provide lower final temperatures and robust cooling even for higher initial temperatures. We estimate that these future improvements could allow reaching average radial and axial motional occupations of $\bar{n}_r = \mathcal{O}(0.01)$ and $\bar{n}_z = \mathcal{O}(0.1)$, respectively, even without further axial confinement (Supplementary Information Section VI).

The motional entropy also allows us to quantify the efficiency of our Raman cooling scheme. In evaporative cooling of atomic and molecular gases, a common efficiency metric is $\gamma = -d \ln(PSD)/d \ln(N)$ where N is the particle number and PSD is the phase space density $^{45-48}$. One can generalize this metric to $\gamma_q = ds/d \ln(N)$, where s is the motional entropy per particle (Supplementary Information Section VII). γ_q coincides with γ in the classical regime and is convenient when in the highly quantized regime. Using our loss measurements, we estimate that $\gamma_q = 70(28)$ for RAC, indicating highly efficient cooling with little loss.

Our demonstration of RSC of molecules in this work opens up several new possibilities. In the near term, the lower temperatures achieved could substantially improve rotational coherence times to the second scale²⁴ and provide more coherent dipolar interactions between molecules. This could enable two-qubit gates with fidelities of more than 0.95 (refs. 22,23) and simulation of quantum spin models into long times ($\mathcal{O}(10^2)$ interaction times). Longer term, our work opens the door to direct laser-cooling of trapped molecules to their three-dimensional motional ground states. This would be a key step towards full quantum control of molecules and could enable efficient production of ensembles with low motional entropy suited for quantum simulation of itinerant and long-range interacting systems in the single-band Hubbard regime. Potentially, RSC could provide an all-optical route towards quantum degeneracy^{36,37} that may be

broadly applicable to other laser-coolable molecules including polyatomic ones^{13,49,50}.

Note: after completion of this work and while the manuscript was under review, related work demonstrating RSC of CaF⁵¹ was reported.

Online content

Any methods, additional references, Nature Portfolio reporting summaries, source data, extended data, supplementary information, acknowledgements, peer review information; details of author contributions and competing interests; and statements of data and code availability are available at https://doi.org/10.1038/s41567-023-02346-3.

References

- DeMille, D. Quantum computation with trapped polar molecules. Phys. Rev. Lett. 88, 067901 (2002).
- Carr, L. D., DeMille, D., Krems, R. V. & Ye, J. Cold and ultracold molecules: science, technology and applications. New J. Phys. 11, 055049 (2009).
- 3. Bohn, J. L., Rey, A. M. & Ye, J. Cold molecules: progress in quantum engineering of chemistry and quantum matter. Science **357**, 1002–1010 (2017).
- Blackmore, J. A. et al. Ultracold molecules for quantum simulation: rotational coherences in CaF and RbCs. Quantum Sci. Technol. 4, 014010 (2018).
- De Miranda, M. H. G. et al. Controlling the quantum stereodynamics of ultracold bimolecular reactions. *Nat. Phys.* 7, 502–507 (2011).
- Liu, Y. et al. Precision test of statistical dynamics with state-to-state ultracold chemistry. Nature 593, 379–384 (2021).
- 7. De Marco, L. et al. A degenerate fermi gas of polar molecules. *Science* **363**, 853–856 (2019).
- Schindewolf, A. et al. Evaporation of microwave-shielded polar molecules to quantum degeneracy. *Nature* 607, 677–681 (2022).
- Barry, J. F., McCarron, D. J., Norrgard, E. B., Steinecker, M. H. & DeMille, D. Magneto-optical trapping of a diatomic molecule. Nature 512, 286–289 (2014).
- Truppe, S. et al. Molecules cooled below the Doppler limit. *Nat. Phys.* 13, 1173–1176 (2017).
- Anderegg, L. et al. Radio Frequency Magneto-Optical Trapping of CaF with High Density. Phys. Rev. Lett. 119, 103201 (2017).
- Collopy, A. L. et al. 3D magneto-optical trap of yttrium monoxide. *Phys. Rev. Lett.* 121, 213201 (2018).
- Vilas, N. B. et al. Magneto-optical trapping and sub-Doppler cooling of a polyatomic molecule. *Nature* 606, 70–74 (2022).
- Cheuk, L. W. et al. Λ-enhanced imaging of molecules in an optical trap. Phys. Rev. Lett. 121, 083201 (2018).
- Caldwell, L. et al. Deep laser cooling and efficient magnetic compression of molecules. *Phys. Rev. Lett.* 123, 033202 (2019).
- Ding, S., Wu, Y., Finneran, I. A., Burau, J. J. & Ye, J. Sub-Doppler cooling and compressed trapping of yo molecules at μk temperatures. *Phys. Rev. X* 10, 021049 (2020).
- Langin, T. K., Jorapur, V., Zhu, Y., Wang, Q. & DeMille, D. Polarization enhanced deep optical dipole trapping of λ-cooled polar molecules. *Phys. Rev. Lett.* 127, 163201 (2021).
- 18. Wu, Y., Burau, J. J., Mehling, K., Ye, J. & Ding, S. High phase-space density of laser-cooled molecules in an optical lattice. *Phys. Rev. Lett.* **127**, 263201 (2021).
- 19. Hallas, C. et al. Optical trapping of a polyatomic molecule in an ℓ -type parity doublet state. *Phys. Rev. Lett.* **130**, 153202 (2023).
- 20. Anderegg, L. et al. Laser cooling of optically trapped molecules. *Nat. Phys.* **14**, 890–893 (2018).
- Anderegg, L. et al. An optical tweezer array of ultracold molecules. Science 365, 1156–1158 (2019).

- Holland, C. M., Lu, Y. & Cheuk, L. W. On-demand entanglement of molecules in a reconfigurable optical tweezer array. *Science* 382, 1143–1147 (2023).
- Bao, Y. et al. Dipolar spin-exchange and entanglement between molecules in an optical tweezer array. Science 382, 1138–1143 (2023).
- 24. Burchesky, S. et al. Rotational coherence times of polar molecules in optical tweezers. *Phys. Rev. Lett.* **127**, 123202 (2021).
- Heinzen, D. J. & Wineland, D. J. Quantum-limited cooling and detection of radio-frequency oscillations by laser-cooled ions. *Phys. Rev. A* 42, 2977–2994 (1990).
- Monroe, C. et al. Resolved-sideband raman cooling of a bound atom to the 3D zero-point energy. *Phys. Rev. Lett.* 75, 4011–4014 (1995).
- Hamann, S. E. et al. Resolved-sideband raman cooling to the ground state of an optical lattice. *Phys. Rev. Lett.* 80, 4149–4152 (1998).
- Kerman, A. J., Vuletić, V., Chin, C. & Chu, S. Beyond optical molasses: 3D Raman sideband cooling of atomic cesium to high phase-space density. *Phys. Rev. Lett.* 84, 439–442 (2000).
- 29. Kaufman, A. M., Lester, B. J. & Regal, C. A. Cooling a single atom in an optical tweezer to its quantum ground state. *Phys. Rev. X* 2, 041014 (2012).
- Thompson, J. D., Tiecke, T. G., Zibrov, A. S., Vuletić, V. & Lukin, M. D. Coherence and raman sideband cooling of a single atom in an optical tweezer. *Phys. Rev. Lett.* 110, 133001 (2013).
- 31. Cheuk, L. W. et al. Quantum-gas microscope for fermionic atoms. *Phys. Rev. Lett.* **114**, 193001 (2015).
- 32. Parsons, M. F. et al. Site-resolved imaging of fermionic ⁶Li in an optical lattice. *Phys. Rev. Lett.* **114**, 213002 (2015).
- 33. He, X. et al. Coherently forming a single molecule in an optical trap. *Science* **370**, 331–335 (2020).
- 34. Zhang, J. T. et al. An optical tweezer array of ground-state polar molecules. *Quantum Sci. Technol.* **7**, 035006 (2022).
- 35. Ruttley, D. K. et al. Formation of ultracold molecules by merging optical tweezers. *Phys. Rev. Lett.* **130**, 223401 (2023).
- Hu, J. et al. Creation of a bose-condensed gas of 87Rb by laser cooling. Science 358, 1078–1080 (2017).
- Urvoy, A., Vendeiro, Z., Ramette, J., Adiyatullin, A. & Vuletió, V. Direct laser cooling to Bose–Einstein condensation in a dipole trap. Phys. Rev. Lett. 122, 203202 (2019).
- 38. Caldwell, L. & Tarbutt, M. R. Sideband cooling of molecules in optical traps. *Phys. Rev. Res.* **2**, 013251 (2020).
- Holland, C. M., Lu, Y. & Cheuk, L. W. Bichromatic imaging of single molecules in an optical tweezer array. *Phys. Rev. Lett.* 131, 053202 (2023).
- 40. Cooper, A. et al. Alkaline-earth atoms in optical tweezers. *Phys. Rev. X* **8**, 041055 (2018).
- 41. Tuchendler, C., Lance, A. M., Browaeys, A., Sortais, Y. R. P. & Grangier, P. Energy distribution and cooling of a single atom in an optical tweezer. *Phys. Rev. A* **78**, 033425 (2008).
- Zhang, X. et al. Subrecoil clock-transition laser cooling enabling shallow optical lattice clocks. *Phys. Rev. Lett.* 129, 113202 (2022).
- 43. Yu, Y. et al. Motional-ground-state cooling outside the Lamb-Dicke regime. *Phys. Rev. A* **97**, 063423 (2018).
- Spence, S., Brooks, R. V., Ruttley, D. K., Guttridge, A. & Cornish, S. L. Preparation of 87Rb and 133Cs in the motional ground state of a single optical tweezer. New J. Phys. 24, 103022 (2022).
- 45. Ketterle, W. & Van Druten, N. J. in *Advances in Atomic, Molecular, and Optical Physics*, Vol. 37 (eds Bederson, B. & Walther, H.) 181–236. (Elsevier, 1996).
- Li, J. R. et al. Tuning of dipolar interactions and evaporative cooling in a three-dimensional molecular quantum gas. *Nat. Phys.* 17, 1144–1148 (2021).

- Bigagli, N. et al. Collisionally stable gas of bosonic dipolar ground-state molecules. Nat. Phys. 19, 1579–1584 (2023).
- 48. Lin, J. et al. Microwave shielding of bosonic narb molecules. *Phys. Rev. X* **13**, 031032 (2023).
- 49. Kozyryev, I. et al. Sisyphus laser cooling of a polyatomic molecule. *Phys. Rev. Lett.* **118**, 173201 (2017).
- 50. Mitra, D. et al. Direct laser cooling of a symmetric top molecule. *Science* **369**, 1366–1369 (2020).
- Bao, Y. et al. Raman sideband cooling of molecules in an optical tweezer array to the 3-D motional ground state. Preprint at https:// doi.org/10.48550/arXiv.2309.08706 (2023).

Publisher's note Springer Nature remains neutral with regard to jurisdictional claims in published maps and institutional affiliations.

Springer Nature or its licensor (e.g. a society or other partner) holds exclusive rights to this article under a publishing agreement with the author(s) or other rightsholder(s); author self-archiving of the accepted manuscript version of this article is solely governed by the terms of such publishing agreement and applicable law.

© The Author(s), under exclusive licence to Springer Nature Limited 2024

Methods

Preparation of molecules

CaF molecules in the $X^2\Sigma(v=0,N=1)$ manifold are created in a single-stage cryogenic buffer gas cell⁵², slowed by means of chirped slowing and loaded into a d.c. magneto-optical trap (MOT). The MOT is subsequently switched off, Λ -cooling is applied and the molecules are loaded into an optical dipole trap (ODT) with the aid of a repulsive ring trap in the presence of Λ -cooling⁵³. The molecules are optically transported and loaded into a reconfigurable array of 37 optical tweezers, which are created with focused laser beams of 781 nm light projected vertically through a microscope objective³⁹. For normalization, after tweezer loading, the occupation of the tweezers is detected non-destructively with Λ -imaging²². After non-destructive detection, the molecules are spread out over all 12 hyperfine states in the $X^2\Sigma(v=0,N=1)$ manifold.

State-resolved detection

To probe the population in $|\downarrow\rangle$, we first lower the trap depth to $U_{\rm MW}=k_{\rm B}\times 130(3)~\mu{\rm K}$ and rotate the magnetic field $(B=4.4~{\rm G})$ to $\theta=53^{\circ}$. Microwaves at ~20.5 GHz are used to transfer the population from $|\downarrow\rangle=|N=1,J=3/2,F=1,m_{\rm F}=0\rangle$ to $|N=0,J=1/2,F=1,m_{\rm F}=-1\rangle$ by means of a Landau–Zener sweep. A pulse of light resonant with the ${\rm X}^2$ $\Sigma(\nu=0,N=1)\to {\rm A}^2\Pi_{1/2}(\nu=0,J=1/2,+)$ transition removes any molecules remaining in ${\rm X}^2\Sigma(\nu=0,N=1)^{22,3^9}$. A second Landau–Zener microwave sweep transfers molecules into $|N=1,J=1/2,F=0,m_{\rm F}=0\rangle$. The two Landau–Zener sweeps have efficiencies of 98% and 99%, respectively. There is minimal loss from the resonant light pulse. Finally, the population is measured by means of Λ -imaging 14 , which detects all molecules in ${\rm X}^2\Sigma(\nu=0,N=1)$. An analogous approach is used to measure population in $|\uparrow\rangle$.

Optical pumping

For optical pumping at $\theta=0^\circ$, we use a single laser beam (OP) in the radial (horizontal) plane containing light addressing the $X^2\Sigma(v=0,N=1) \rightarrow A^2\Pi_{1/2}(v=0,J=1/2,+)$ transition ($\lambda=606.3$ nm). The beam has frequency components resonant with all four resolved hyperfine transitions. The beam makes an angle of 42° relative to the tweezer polarization axis $\hat{\epsilon}(\hat{x})$. It is optimized to have minimal σ_+ component along the quantization axis set by the magnetic field (along \hat{x} at $\theta=0^\circ$). For the data exploring optical pumping at the magic angle $\theta=\theta_{\rm m}$ (Fig. 2b,c), we use a second optical pumping beam (OP2) propagating along \hat{y} . This beam is optimized to have minimal σ_+ component along the quantization axis set by the magnetic field.

Raman coupling

To achieve Raman coupling between $|\uparrow\rangle$ and $|\downarrow\rangle$, we use light with two frequency components ω_1 and ω_2 detuned near the $X^2\Sigma(v=0,N=1) \rightarrow B^2\Sigma(v=0,N=0)$ transition ($\lambda=531.0$ nm) with a single-photon detuning of $\Delta=-2\pi\times42$ GHz. $\omega_1(\omega_2)$ nominally couples to $|\uparrow\rangle(|\downarrow\rangle)$. These components are generated by acousto-optical modulators, allowing the two-photon detuning δ to be varied.

To achieve motional coupling in the radial (horizontal) xy-plane, we send beams R_1 and R_2 along the $\hat{x}+\hat{y}$ and $\hat{x}-\hat{y}$ directions, respectively. R_1 (R_2) carries a single frequency component ω_1 (ω_2), is linearly polarized vertically along \hat{z} and has a $1/e^2$ beam waist of -0.3 mm. The two radial beams are optionally retro-reflected off piezo-modulated mirrors to address two orthogonal radial directions. The positions of the two mirrors are modulated over -1 μ m sinusoidally at frequencies of 355 Hz and 500 Hz to partially counteract inhomogeneous Raman coupling and a.c. Stark shifts due to interference of the Raman beams. The retro-reflections are controlled by shutters that can be controlled on slow (-10 ms) timescales mid-sequence. To address axial motion, we send beams R_3 and R_4 along $-\hat{z}$ and \hat{z} , respectively. R_3 is linearly polarized along \hat{y} , whereas R_4 is linearly polarized perpendicular to $\theta = \theta_m$. R_4 has a $1/e^2$ beam waist of -0.4 mm. The power of R_3 , which goes

through a microscope objective, is adjusted so that the intensities of R_3 and R_4 are balanced at the tweezer locations. This is accomplished experimentally by matching the observed loss rates due to off-resonant scattering from either R_3 or R_4 alone.

Spectroscopy sequences

We use the following sequence for the data presented in Fig. 2a. First, molecules are pumped into $|\uparrow\rangle$ by turning on OP for 2 ms in a bias magnetic field of B=4.4 G at $\theta=0^\circ$. Next, the tweezer depth is decreased to $U_{\rm R}$ and the magnetic field is rotated to the desired angle θ . Both ω_1 and ω_2 are delivered through a single vertical beam R_4 along the tweezer axis, and each component has a power of 1.1 mW (2.0 mW) for carrier spectroscopy in the $\theta=\theta_{\rm m}$ ($\theta=0^\circ$) configuration. A Raman pulse is applied for 170 $\mu{\rm s}$ with an estimated two-photon Rabi coupling of $\Omega_{\rm R}\approx 2\pi\times 3$ kHz in the 0° configuration. Finally, the population in $|\downarrow\rangle$ is measured.

For all spectra in Figs. 3 and 4, the radial Raman beams R_1 and R_2 are not retro-reflected, to minimize carrier transfer, inhomogeneous Raman coupling and light shifts induced by the Raman beams. All spectra in Fig. 3 are taken in a bias field of B = 4.4 G at $\theta = 0^\circ$. For the radial spectrum in Fig. 3a, radial beams R_1 and R_2 are applied for 1 ms, probing the radial direction \hat{y} , and contain 1.8 mW and 1.9 mW of optical power, respectively. For the axial spectrum in Fig. 3b, ω_1 is delivered through R_3 and ω_2 through R_4 , and the beams are applied for 1 ms. R_4 has a total power of 3.3 mW, and R_3 has a matched intensity.

All spectra in Fig. 4 are taken in a magnetic field of B=5.5 G at $\theta=\theta_{\rm m}$. For radial spectra in Fig. 4a,c, R_1 and R_2 are used and contain 7.1 mW and 7.0 mW of optical power, respectively. The beams are applied for 30 µs (carrier) or 50 µs ($\Delta n_{\rm r}=\pm 1$ sidebands), with $\Omega_{\rm R}\approx 2\pi\times 20$ kHz. For axial spectra in Fig. 4b,d, ω_1 is delivered through R_3 and ω_2 is delivered through R_4 . R_4 has 10 mW of optical power, and R_3 has matching intensity with R_4 . The beams are applied for 100 µs, with an estimated Rabi frequency of $\Omega_{\rm R}\approx 2\pi\times 20$ kHz.

Cooling sequences

Before RSC, we optically pump molecules into $|\uparrow\rangle$ by applying OP for 2 ms. OP has a waist $(1/e^2$ radius) of ~0.65 mm and contains a total power of 7.8 μ W during optical pumping.

For the RAC sequence, both radial beams R_1 and R_2 are on and retro-reflected. They contain 3.3 mW and 5.2 mW of optical power, respectively. Axially, we send ω_1 into R_3 , and ω_2 into R_4 . R_4 contains 3.5 mW of optical power. The power of R_3 is adjusted to match the intensity of R_4 . All Raman beams are applied simultaneously. Raman transfer is performed with light resonant with the radial $\Delta n_r = -2$ (axial $\Delta n_z \approx -9$) sideband for 150 μ s, and optical pumping with OP for 150 μ s. The Raman transfer occurs at tweezer depth U_R , and the optical pumping occurs at depth U_0 . The tweezer depth ramps occur over 200 μ s between each of these steps.

For the IRC sequence, we turn on the radial beams R_1 and R_2 only, with R_1 retro-reflected. When addressing the $\Delta n_r = -2$ sideband, the powers in R_1 and R_2 are identical to those used in RAC. When addressing the $\Delta n_r = -1$ sideband, the powers in R_1 and R_2 are intentionally imbalanced (2.2 mW and 11.0 mW, respectively) to minimize off-resonant transfer on the carrier transition. Raman transfer on the $\Delta n_r = -2$ ($\Delta n_r = -1$) sideband occurs for 150 μ s (300 μ s).

Data availability

Data for figures in the Supplementary Information are available from Dryad⁵⁴. Additional experimental data are available from the corresponding authors upon reasonable request. Source data are provided with this paper.

Code availability

The code used in this manuscript is available from the corresponding author upon reasonable request.

References

- 52. Hutzler, N. R., Lu, H. I. & Doyle, J. M. The buffer gas beam: an intense, cold, and slow source for atoms and molecules. *Chem. Rev.* **112**. 4803–4827 (2012).
- 53. Lu, Y., Holland, C. M. & Cheuk, L. W. Molecular laser cooling in a dynamically tunable repulsive optical trap. *Phys. Rev. Lett.* **128**, 213201 (2022).
- Lu, Y., Li, S. J., Holland, C. M. & Cheuk, L. W. Data for: Raman sideband cooling of molecules in an optical tweezer array (dryad). *Dryad* https://doi.org/10.5061/dryad.tht76hf4g (2023).

Acknowledgements

We thank J. Thompson, W. Bakr and the Bakr group for fruitful discussions. This work is supported by the National Science Foundation (grant no. 2207518) and by the Sloan Research Foundation (grant no. FG-2022-19104). C.M.H. acknowledges support from a Joseph Taylor Graduate Student Fellowship. S.J.L. acknowledges support from a Princeton Quantum Initiative Graduate Student Fellowship.

Author contributions

L.W.C. conceived the study and supervised the experiment. Y.L., C.M.H. and S.J.L. performed the experiments and the data analysis. All authors contributed to the manuscript.

Competing interests

The authors declare no competing interests.

Additional information

Supplementary information The online version contains supplementary material available at https://doi.org/10.1038/s41567-023-02346-3.

Correspondence and requests for materials should be addressed to Lawrence W. Cheuk.

Peer review information *Nature Physics* thanks Andreas Schindewolf, Hannah Williams and the other, anonymous, reviewer(s) for their contribution to the peer review of this work.

Reprints and permissions information is available at www.nature.com/reprints.